

LETTER TO THE EDITOR

Search and analysis of giant radio galaxies with associated nuclei (SAGAN)

IV. Interplay with the Supercluster environment

Shishir Sankhyayan^{1*} and Pratik Dabhade^{2,3**}

¹Tartu Observatory, University of Tartu, Observatooriumi 1, 61602 Tõravere, Estonia

²Instituto de Astrofísica de Canarias, Calle Vía Láctea, s/n, E-38205, La Laguna, Tenerife, Spain

³Universidad de La Laguna (ULL), Departamento de Astrofísica, La Laguna, E-38206, Tenerife, Spain

June 25, 2024

ABSTRACT

We investigated the prevalence of giant radio galaxies (GRGs), some of the largest structures powered by supermassive black holes, within supercluster environments, and the influence of such environments on their properties. Utilising two large catalogues of superclusters (401) and GRGs (1446), we established the existence of 77 GRGs (5.3%) residing in 64 superclusters (16%) within $0.05 \leq z \leq 0.42$. Among the 77 GRGs found in superclusters, we identified $\sim 70\%$ as residing within galaxy clusters. Within the subset of GRGs not located in superclusters, which constitutes 94.7% of the sample, a mere 21% are associated with galaxy clusters, while the remaining majority are situated in sparser environments. We examined the influence of differing environments, such as cluster versus non-cluster and supercluster versus non-supercluster regions, on the size of GRGs, while also exploring the driving factors behind their overall growth. Our findings show that the largest GRGs (≥ 3 Mpc) grow in underdense environments beyond the confines of dense environments. Moreover, we show that $\sim 24\%$ of 1446 GRGs reside in galaxy clusters. We conclude that GRGs preferentially grow in sparser regions of the cosmic web and have a significantly larger median size. Finally, we demonstrate the potential of GRGs as astrophysical probes with specific cases where GRGs, exhibiting polarised emissions and located behind superclusters (acting as natural Faraday screens), were used to estimate magnetic field strengths of the supercluster environment at sub-microgauss levels.

Key words. magnetic fields – galaxies: active – galaxies: clusters: general – large-scale structure of Universe – radio continuum: galaxies

1. Introduction

The matter in the Universe is distributed in an intricate network called the cosmic web (Einasto et al. 1980; Bond et al. 1996), composed of clusters, filaments, sheets, and voids. Nested within these are superclusters (SCs), vast conglomerates of galaxies and clusters with higher number densities than the universal average, spanning tens to hundreds of megaparsecs (Mpc) in size (e.g. Lietzen et al. 2016; Bagchi et al. 2017). The densities within these massive structures are not uniform, but are instead influenced by the spatial distribution of their constituent galaxies and clusters (Liivamägi et al. 2012).

Recent studies by Sankhyayan et al. (2023) and Einasto et al. (2024) highlight the supercluster environment's influence on the growth of galaxy groups and clusters. These groups and clusters, on Mpc scales, are impacted by the environments of SCs with sizes ranging from tens to hundreds of Mpc. Given the scales involved and the dynamical nature of these superstructures, it stands to reason to investigate whether similarly vast entities on Mpc scales, such as giant radio galaxies (GRGs) with projected linear sizes ≥ 0.7 Mpc, are also subject to the influence of their supercluster habitats.

Giant radio galaxies are a subclass of radio sources powered by supermassive black holes (SMBHs). Their large sizes are inferred to result from extensive jets reaching Mpc scales (for a review, see Dabhade et al. 2023), though these jets are not often detected in radio images, especially in the most common type of GRGs, the FRIIs (Fanaroff & Riley 1974). Until recently, the prevalence of GRGs was perceived to be substantially lower compared to typical radio galaxies (normal-sized), and the explanations for their immense size were largely conjectural. The scarcity of a statistically significant sample of GRGs hindered a thorough investigation. Recent advancements in large sky area radio surveys (e.g. LOFAR Shimwell et al. 2022) have enabled considerable progress in identifying and comprehensively investigating large samples of GRGs (e.g. Dabhade et al. 2020c; Oei et al. 2023a). While the radio properties and broader active galactic nucleus (AGN) characteristics of GRGs have been extensively studied (e.g. Konar et al. 2004; Dabhade et al. 2020b; Kuźmicz et al. 2019; Dabhade et al. 2020a, and references therein), fewer studies have been conducted on their large-scale environmental properties (e.g. Komberg & Pashchenko 2009; Lan & Prochaska 2021; Oei et al. 2024). One prevailing hypothesis posits that GRGs predominantly grow in environments with a sparser (e.g. Mack et al. 1998) intergalactic medium (IGM). With the recent increment in the availability of large GRG samples, we can now more effectively study the local and broader

* e-mail: shishir.sankhyayan@ut.ee

** e-mail: pratik.dabhade@iac.es

environments that influence GRGs. Understanding these environments is crucial to unravelling the growth, formation, and evolution of GRGs. The substantial sizes of GRGs are attributed to their powerful jets, which are likely to influence the properties of their host AGNs and galaxies. Consequently, the study of GRGs is crucial for advancing our understanding of AGN feedback mechanisms.

Recently, [Oei et al. \(2023b\)](#) used radio and X-ray data combined with modelling of GRG (NGC 6185) to estimate the temperature of the warm-hot intergalactic medium (WHIM), demonstrating that GRGs can probe the thermodynamics of galaxy groups and beyond. Their results highlight the importance of GRGs as cosmic probes within supercluster environments, marking a significant advancement in their utility.

The potential for SCIs to impact the development and characteristics of GRGs forms the basis of our inquiry, bridging the gap between the largest scale structures in the Universe and the largest jets (and their products) powered by SMBHs. GRGs, owing to their large sizes and luminous radio emission, can serve as tools for exploring other astrophysical processes. The following points highlight the possible pivotal roles of GRG.

Firstly, GRGs, with their large jets and lobes, are crucial for studying galaxy evolution, particularly in supercluster environments; probing the Universe’s large-scale structure; and understanding the shape, composition, and evolution of the cosmic web through their interactions with superclusters. Additionally, by mapping the IGM, GRGs can possibly help address the ‘missing baryon problem’. Secondly, GRGs are important for mapping magnetic fields. Once identified in SCIs, the extensive lobes of GRGs can be studied through multi-frequency radio observations to measure magnetic field strengths within these structures. The lobes of GRGs, extending through the IGM, offer insights into magnetic field structures across superclusters. Their large-scale radio emissions make them excellent probes for the magnetic environments in these dense regions. Additionally, identifying GRGs behind superclusters enables probing of the magnetic field through the Faraday rotation method.

To address these points, it is crucial first to identify a statistically significant sample of GRGs within (as well as behind) supercluster environments. Thus, under the project SAGAN¹ ([Dabhade et al. 2017, 2020b](#)), our aim is to systematically study the large-scale environment of GRGs, specifically focusing on quantifying the presence of GRGs in the densest and the largest regions of the Universe, such as SCIs. We compare the properties of GRGs within superclusters to those outside, examining how their size, radio morphology, and spectral characteristics are influenced by their environment. Factors like their supercluster location can affect their morphology, leading to potential distortions, and may correlate with their current state of activity, whether active or relic (discernible from their radio structure and spectral features). This investigation is vital for revealing how environmental factors impact the lifecycle of GRGs.

The study by [Mauduit & Mamon \(2007\)](#) is a notable exception in the extremely limited research examining radio galaxies in the context of their supercluster environment and its effects on them. Their study on the Shapley Supercluster ([Raychaudhury 1989](#)) found that the dense core regions, where clusters are merging, have the fewest radio galaxies or sometimes none at all. They suggest that this is likely due to the disruption of their fuel supply (for feeding SMBHs) caused by major mergers between clusters. When considering GRGs, the findings to date have been minimal, with only one identified in the Horologium-Reticulum

Supercluster ([Safouris et al. 2009](#)) and two in the Supercluster XLSSsC N03 ([Horellou et al. 2018](#)).

Throughout this paper, we adopted the flat Λ cold dark matter (Λ CDM) cosmology with the following cosmological parameters: $H_0 = 67.66 \text{ km s}^{-1} \text{ Mpc}^{-1}$, $\Omega_{m0} = 0.3111$, and $\Omega_{\Lambda0} = 0.6889$ ([Planck Collaboration et al. 2020](#)).

2. Giant radio galaxy and supercluster data

Giant radio galaxy data: We utilised the GRG catalogues of [Dabhade et al. \(2020c\)](#) and [Oei et al. \(2023a\)](#), derived from wide-sky area LoFAR Two Metre Sky Survey (LoTSS; [Shimwell et al. 2022](#)), along with GRG catalogues derived from LoFAR deep field surveys ([Simonte et al. 2022, 2023](#)). These radio surveys have excellent sensitivity to diffuse radio emission. Given the depth of the surveys and the meticulous validation process, these catalogues can be considered robust and comprehensive. Since the GRGs reported by all the above-mentioned catalogues are exclusively new discoveries, we retrieved additional GRGs documented in the literature corresponding to the sky area covered by LoTSS, through the SAGAN ([Dabhade et al. 2020b](#)) catalogue² as it is a compendium of all GRGs reported till 2020. For our study, we amalgamated all these resources to formulate an enhanced GRG-catalogue. Subsequently, we applied specific redshift and sky area filters to align this GRG-catalogue with the supercluster catalogue, thereby facilitating a more targeted and effective analysis of GRGs within these overdense regions (see Sect. 3).

Supercluster data: We utilised the supercluster catalogue (SCI-catalogue) of [Sankhyayan et al. \(2023\)](#) (hereafter SSC23) with 662 SCIs. They identified SCIs by applying a modified friends of friends (FoF) algorithm on the cluster catalogue of [Wen & Han \(WH15, 2015\)](#), which is based on the SDSS DR12 ([Alam et al. 2015](#)). They found that in a supercluster environment, member clusters are more massive (high richness) compared to clusters in a non-supercluster environment, indicating the influence of the supercluster environment on their evolution. They showed that a supercluster has a gravitational influence on its constituents visible in the phase-space distribution of the mock SCIs extracted from the Horizon Run 4 (HR4, [Kim et al. 2015](#)) simulation. In this catalogue, the median mass of SCIs is $\sim 5.8 \times 10^{15} M_{\odot}$ and the median size is $\sim 65 \text{ Mpc}$ (SSC23). The advantage of using the catalogue of SSC23 is its wide sky-area coverage ($\sim 14000 \text{ deg}^2$) and relatively large redshift span ($0.05 \leq z \leq 0.42$). In addition, this catalogue also provides the masses and density contrast (δ) of SCIs. In contrast to other catalogues (e.g. [Liu et al. 2024](#)) that classify even cluster pairs as superclusters, SSC23 identifies superclusters with at least ten member clusters. This is made feasible by the comprehensiveness of the WH15 catalogue. Defining supercluster boundaries in 3D space with only two to three member clusters is very challenging, as is identifying GRGs within them.

3. Identifying giant radio galaxies in superclusters and clusters

Ensuring a fair cross-matching between the GRG-catalogue and the SCI-catalogue requires finding the common sky coverage and redshift span in the two datasets. Moreover, for the purpose of investigating potential distinctions in the properties of SCIs hosting GRGs compared to those without any GRGs

² <https://vizier.cds.unistra.fr/viz-bin/VizieR-3?-source=J/A%2bA/642/A153/grs>

¹ <https://sites.google.com/site/anantasakyatta/sagan>

(see Sect. 4), it is crucial to exclude sky regions containing SCIs but without the sky coverage of the GRG-catalogue. This process involves exclusively considering GRGs within the sky-coverage mask defined by the input cluster catalogue used to make the SCI-catalogue, as detailed in SSC23. The sky mask is generated using a Healpix map with a resolution parameter of $N_{side} = 64$. Pixels harbouring at least one cluster are assigned a value of 1, while those devoid of clusters receive a value of 0. A similar procedure is employed to generate a sky mask for the GRG-catalogue; however, a reduced resolution of $N_{side} = 16$ is used to accommodate the lower number density of GRGs on the sky-plane compared to clusters. The intersection of these two masks defines the region of interest for our study (see Fig. A.1). Additionally, a redshift constraint of $0.05 \leq z \leq 0.42$ is implemented on the GRG-catalogue to align its redshift span with that of the SCI-catalogue. These constraints give a GRG-sample of 1446 and a SCI-sample of 401 SCIs.

Given the complex geometries of SCIs, delineating their boundaries presents a significant challenge. This challenge is heightened when using the FoF algorithm for supercluster identification as it provides discrete locations for member clusters. Using an ellipsoid fit to define the supercluster boundary may overestimate its volume, while a wrapping method risks underestimation due to the dependence on a parameter determining the extent of wrapping. To strike a balance, we adopted the convex hull of member clusters as the supercluster boundary.

In 3D Euclidean space, the convex hull of a set of points \mathbf{P} represents the minimum-volume convex surface encompassing \mathbf{P} (Barber et al. 1996). To locate GRGs within a supercluster boundary, we cross-matched the GRG-sample with the SCI-sample, identifying GRGs within the convex hull region formed by the member clusters of a supercluster (see Fig. 1 for an example). SSC23 also used the convex hull of member clusters to estimate the SCI volumes and subsequently calculated their densities (or density contrast). This approach supports the use of a convex hull for boundary estimation in this study, particularly when investigating the properties of SCIs hosting GRGs compared to those without GRGs.

We also located GRGs within or outside galaxy clusters (CIs) using the cluster catalogue of Wen & Han (2015), while also suppressing the fingers-of-god redshift distortion induced by peculiar velocities of galaxies within clusters (Jackson 1972). First, we identified all GRGs in the GRG-sample, irrespective of their SCI environment, within the projected cluster radius on the sky plane and falling within a certain redshift range determined by the cluster’s velocity dispersion. Then, these GRGs were labelled as being in the CI environment, and their fingers-of-god redshift distortion was suppressed accordingly. The details of this method are presented in Appendix B.

4. Results: The influence of environment on the sizes of giant radio galaxies

We used the GRG-sample of 1446 GRGs for the analysis of their large-scale environments. As mentioned in Sect. 3, we also identified GRGs that are members of clusters both inside and outside of SCI environments. We found that $\sim 24\%$ GRGs are in galaxy clusters (see Table 1), which is similar to the finding of Oei et al. (2024) for lower redshifts ($z < 0.16$). Our analysis shows that GRGs associated with galaxy clusters have a median size of 1.1 Mpc, regardless of their supercluster environment, while those in non-cluster environments have a slightly larger median size

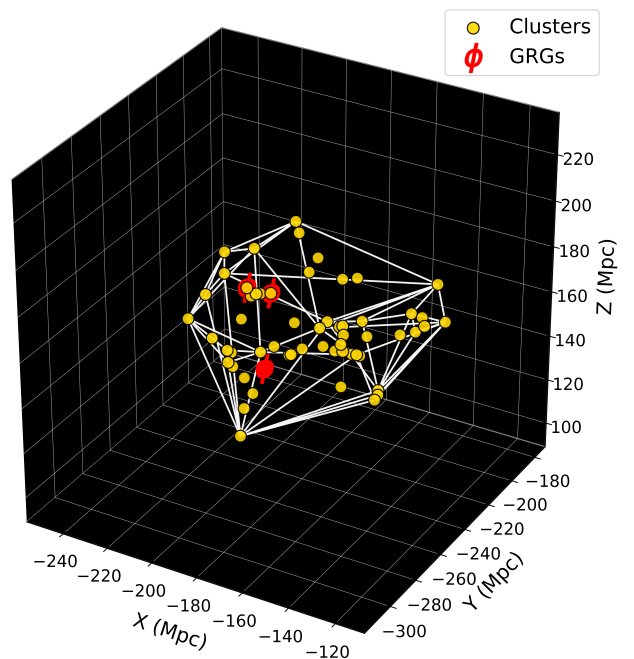


Fig. 1: Three GRGs (red markers) inside SCI 2. Two of the GRGs are the brightest cluster galaxies. Here, the supercluster SCI 2 is represented by convex hull edges (white lines), encompassing its 57 member galaxy clusters shown in yellow (see Sect. 3 and Table E.1 for more details). X, Y, and Z are the equatorial co-moving coordinates.

of 1.2 Mpc. We conducted a non-parametric Mann-Whitney U test to compare these sample medians ($W = 171757$, $p = 0.007$), indicating a significant difference in the median sizes of GRGs between cluster and non-cluster environments.

The distribution of GRGs and their sizes from the GRG-sample across various environments is presented in Table 1 and Fig. 2, respectively, to assess which favours their growth. Below, we present our key findings:

- Approximately 95% of GRGs³ are located outside supercluster environments. Fig. 2 clearly shows that the largest (≥ 3 Mpc) GRGs grow in relatively isolated environments beyond the confines of SCIs or galaxy clusters. The majority of the GRGs from the GRG-sample are outside SCIs, and of these $\sim 21\%$ evidently grow in galaxy clusters (see Table 1).
- Using the information about the extent and overall geometry of superclusters and their constituent member galaxy clusters, we present for the first time the distribution of GRGs in the complex architecture of SCIs (see Fig. 1). A mere 5.3% (77 GRGs) of GRGs, with a median size of ~ 1.1 Mpc, are located within superclusters (listed in Table E.1), suggesting that supercluster environments likely impose a restrictive influence on the growth of GRGs, as indicated by their limited presence and smaller median size (see Fig. 2). In this subset of GRGs found in SCIs, $\sim 70\%$ (47 BCGs and 7 galaxy cluster members) reside in galaxy clusters (see Col. 13 of Table E.1) and 23 are located outside of galaxy clusters.

³ The relevant data tables of GRGs in non-supercluster environments, including their cluster and non-cluster associations, will be made available through VizierR.

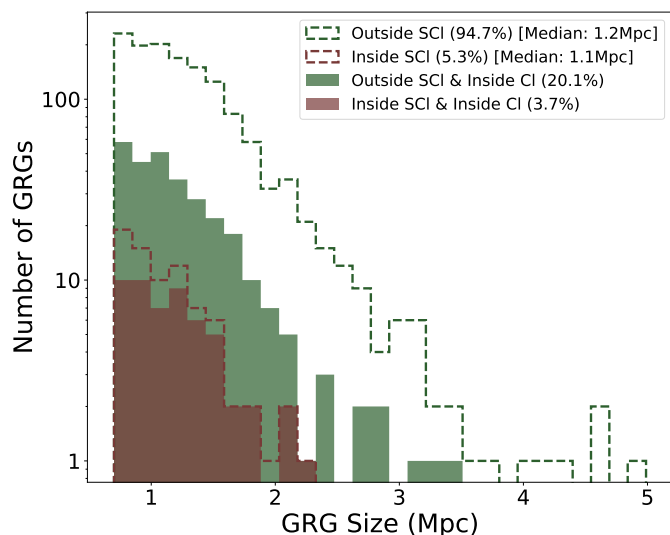


Fig. 2: Size distribution of GRGs. The green dashed line shows GRGs outside superclusters; the green solid histogram represents those outside superclusters but within clusters. The brown dashed line indicates GRGs within superclusters, and the brown solid histogram shows GRGs within both superclusters and clusters. The percentages and median sizes of GRGs inside and outside SCIs are also shown in the legend.

4.1. Variations in giant radio galaxy properties: A statistical analysis of supercluster associations

To probe for variations in GRG attributes contingent on their supercluster association, we conducted a two-sample Kolmogorov-Smirnov (KS) test. This analysis focused on three key aspects: the size distribution of GRGs inside versus outside SCIs, the mass of the central SMBHs within these GRGs, and the density contrasts of SCIs that host GRGs compared to those that do not. The KS test evaluates the null hypothesis that the two samples originate from identical distributions. The null hypothesis is rejected if the p-value of the KS test is > 0.05 . The parameters of the KS test are presented in Table 2. Here we discuss the outcomes of the test and their implications.

We observe significant size differences between GRGs within and outside SCIs, which is also seen in Fig. 2 (distributions represented by dashed green and dashed brown lines). We observe that GRGs within the confines of SCIs, particularly those in CI environments, predominantly span sizes up to ~ 1.5 Mpc, with an absence of GRGs exceeding ~ 2.5 Mpc. Conversely, GRGs outside of SCI boundaries exhibit a potential for greater expansion, reaching sizes up to ~ 5 Mpc. The distributions conclusively show the constraining effect of SCI environments on the growth of GRGs to larger sizes ($\gtrsim 2$ Mpc).

We compared the masses of SMBHs hosting GRGs located both within SCIs (57/77 GRGs, as per availability of SMBH masses in Oei et al. 2023a) and outside SCIs (683/1369 GRGs). The KS test's p-value of 0.08 (see Table 2) at best suggests marginal evidence that these are drawn from different populations. The median values of the masses of SMBHs inside and outside SCIs are $1.05 \times 10^9 M_{\odot}$ and $9.24 \times 10^8 M_{\odot}$, respectively.

Fig. 3 shows the distribution of density contrast (δ) between superclusters that contain GRGs (red histogram) and those that do not host any GRGs (green histogram). It shows that the location of GRGs is preferentially skewed towards lower-density SCIs (also see Table 2). The presence of GRGs in SCIs with a

Table 1: Percentage of 1446 GRGs from the GRG-sample in different environments.

<i>Environment</i>	<i>Cluster</i>	<i>Non-Cluster</i>
Supercluster	3.7%	1.6%
Non-Supercluster	20.1%	74.6%

Table 2: Detailed statistics of the KS test. More details in Sec. 4.

<i>Samples</i>	<i>Statistic</i>	<i>p-value</i>
GRGs Size (inside and outside SCI)	0.17	0.03
GRGs SMBH Mass (inside and outside SCI)	0.17	0.08
SCIs δ (host and non-host SCI)	0.20	0.02

density contrast $\delta \gtrsim 25$ is markedly rare (only six). Among the 401 superclusters analyzed, only 64 (16%) contain GRGs. This shows that the majority of these large coherent overdense regions within the cosmic web do not facilitate the growth of GRGs.

Our analysis (see Figs. 2 and C.1) also suggests that the densest regions within SCIs, particularly those close to massive and nearby member clusters, are not the most favourable for the formation of the largest GRGs ($\gtrsim 3$ Mpc). These regions could be characterised by more complex gravitational interactions, potentially leading to disruptions in the radio jet propagation that is necessary for GRG growth. Our visual inspection of radio images from LoTSS DR2 data reveals that fewer than 10% of GRGs within SCIs do not show major structural distortions, such as bent lobes or high asymmetry.

4.2. Two exceptional superclusters with giant radio galaxies

We identified two exceptional superclusters, SCI 2 and SCI 73, hosting three GRGs (see Fig. 1 and Table E.1). Notably, SCI 2 is the second most massive ($M \approx 2.55 \times 10^{16} M_{\odot}$) supercluster at $z \approx 0.08$ listed in SSC23, making the presence of three GRGs in this dense environment remarkable. It extends to ≈ 124 Mpc and contains 57 member clusters. SCI 2 is a composite entity of two substantial sub-structures, the Corona Borealis (CB) supercluster and the Abell 2142 supercluster, weakly connected by a chain of galaxies and poor groups (Pillastrini 2019; Einasto et al. 2021). Two of the three GRGs in SCI 2, which are also BCGs, exhibit bent radio morphologies, underscoring the influence of their dynamic local environment. It is often found that the dominant galaxies in clusters or groups are wide-angle tail (WAT) radio sources, known for their powerful, bent emissions (O'Dea & Baum 2023). Similarly, we find three GRGs in SCI 73, which is located at $z \approx 0.14$, has a mass $M \approx 1.02 \times 10^{16} M_{\odot}$, has a spatial extent of ≈ 94 Mpc, and encompasses a total of 21 member galaxy clusters. Furthermore, there are nine other SCIs with two GRGs in each (see Table E.1 for details).

5. Giant radio galaxies as probes of the magnetic field in superclusters

As described in Sect. 1, the objective of identifying GRGs within supercluster environments extends beyond examining the influence of these dense and massive structures on the GRGs themselves. GRGs serve a dual purpose in this context: they are the subjects of study in terms of how extreme environments impact their morphology and evolution, and they are also instrumental as astrophysical probes. It can be inferred from studies (e.g. Strom 1973; O'Sullivan et al. 2018, 2023, and references therein) that large radio galaxies like GRGs show a higher de-

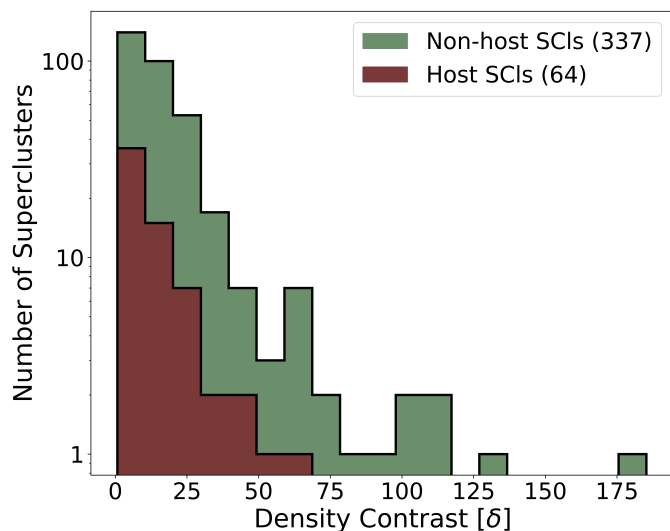


Fig. 3: Distribution of density contrast of SCIs hosting GRGs (64) compared to those that do not host GRGs (337). It indicates that superclusters with high densities impede the growth of a radio galaxy, preventing it from developing into a GRG.

gree of polarisation at low radio frequencies, and hence they can more effectively be used as probes with their Faraday rotation measurements.

We propose here that GRGs offer a unique vantage point when positioned behind SCIs. Utilising linear radio polarisation and Faraday rotation measurements, they become effective tools for constraining the intra-supercluster medium’s magnetic field and thermal electron density (see Fig. D.1). This methodology has been successfully applied to filaments in the cosmic web (e.g. O’Sullivan et al. 2019). Building on this, the recent Faraday rotation measurements (RMs) from O’Sullivan et al. (2023) allow us to infer the magnetic field strength of the supercluster. Since these measurements are based on low-frequency observations, they offer higher precision in RM values and are also more sensitive to weaker magnetic fields, such as those pervasive, possibly in the supercluster environment. From our GRG-sample, we reliably identified eight GRGs located behind SCIs with available RM measurements from O’Sullivan et al. (2023), as listed in Table E.2. We only included GRGs with spectroscopic redshift measurements, non-cluster members, and non-supercluster members (see Sect. 3) to minimize ambiguity and to mitigate the local contribution to the RM values. The polarised emission from the GRGs probes or samples a substantial region ($\Delta L_{\perp, \text{SCI}}$) of the supercluster on the sky plane. The path length ($\Delta L_{\parallel, \text{SCI}}$) within the supercluster, covered by the polarised radio waves from the background GRGs, is estimated by taking the redshift limits (Δz) of the supercluster (i.e. the extent of the supercluster along the direction of the line of sight). Using the NASA Extragalactic Database (NED), we also verified that the polarised emission traverses the intercluster magneto-ionic medium of the supercluster (responsible for the Faraday rotation) and not through any known core regions of galaxy clusters. By assuming negligible background⁴ and foreground effects on RM and adopting electron density (n_e) values of 10^{-6} and 10^{-7}

⁴ In our analysis, we assume that contributions to RM from effects or processes local to the GRG are negligible (unless it is in a CI or SCI). The possible minor local contribution to RM may occur due to various local environment factors as discussed in Rudnick & Blundell (2003).

cm^{-3} (reasonable for the intra-SCI environment), we obtained the magnetic field strengths of sub- μG (for further details, see Appendix D) and these are averaged on scales of $\Delta L_{\perp, \text{SCI}}$ given in Col. 12 of Table E.2. These values are comparable to those obtained by Xu et al. (2006) using similar techniques. Furthermore, using the equipartition method, Venturi et al. (2022) estimated a magnetic field strength of $0.78 \mu\text{G}$ over a scale of ~ 1 Mpc in the Shapley supercluster, which is in a range similar to ours.

In summary, we present a compelling proof of concept for employing GRGs as probes to determine the magnetic field strengths within SCIs, utilising the Faraday rotation measure technique. This novel approach sets the stage for future work, wherein there exists the potential to comprehensively map the magnetic field distributions across entire SCIs, bolstered by improved statistics (e.g. using POSSUM Vanderwoude et al. 2024).

6. Summary

We have presented a comprehensive examination of large-scale environments of GRGs in superclusters and galaxy clusters. We have shown that for the redshift range of $0.05 \leq z \leq 0.42$, only $\sim 16\%$ of superclusters (of only moderate densities) host GRGs, which is only about 5.3% of the GRG-sample, clearly showing that the sparser cosmic web environments favour the growth of GRGs. This is further substantiated by the fact that the largest GRGs (≥ 3 Mpc) are found outside of clusters or superclusters. Our analysis indicates that GRGs in cluster environments are smaller than those in non-cluster environments, regardless of whether the clusters are part of a supercluster. Furthermore, GRGs in cluster environments can grow to sizes ≥ 2 Mpc if the host cluster is not part of a supercluster. However, within superclusters, cluster-GRGs rarely exceed 2 Mpc, highlighting the restrictive influence of supercluster environments.

In non-supercluster environments most GRGs are non-BCGs, whereas in superclusters the majority are BCGs. This finding contrasts with the typical preference of GRGs for sparser environments, highlighting a unique characteristic within superclusters. However, sparse environments are not the sole factor for GRG growth to megaparsec scales; jet kinetic power, dependent on the AGN’s power and accretion state, also plays a crucial role. BCGs, particularly in superclusters, having grown through multiple mergers, are likely to host the most powerful AGNs capable of producing jets that pierce through the dense intracluster medium and intra-supercluster medium, thereby forming GRGs. Additionally, BCGs are more likely to exhibit extended radio emission compared to other cluster members (e.g. Garon et al. 2019), increasing their probability of being GRGs. Also, our findings conclusively show that a majority ($\sim 76\%$ of GRG-sample) of GRGs reside in non-cluster environments, like filaments and voids, which will be further investigated in our future work as part of the SAGAN project.

Moreover, this study has uniquely identified eight GRGs (with RM information) directly behind six superclusters on the sky plane for the first time. Using RM data, we demonstrated their potential to estimate the magnetic field strength in the supercluster’s intercluster medium. This investigation lays the groundwork for further characterising GRGs in various environments and establishes GRGs as powerful probes for exploring astrophysical phenomena, including the magnetised cosmic web.

Overall, this work represents an initial step in identifying the large-scale environments of GRGs and their effects using the best available catalogues of GRGs, galaxy clusters, and superclusters in a statistical manner. Future studies can build on this foundation with improved data, and more detailed investigations

will be possible with upcoming survey data from DESI (DESI Collaboration et al. 2023), *Euclid* (Euclid Collaboration et al. 2019), and 4MOST (de Jong et al. 2019), enhancing the robustness of our findings.

Acknowledgements. We thank the referee for detailed and useful comments on the manuscript. We dedicate this paper to the loving memory of SS's late grandfather (Dr. Narendra Sankhyayan). We also thank Elmo Tempel, Shabbir Sheikh, Maret Einasto and Vikram Khairé for their valuable comments on the manuscript. SS acknowledges the support of the ETAG grant PRG1006 and the HTM project "Foundations of the Universe" (TK202). PD acknowledges support from the Spanish Ministry of Science & Innovation under the grant "PARSEC: Multiwavelength investigations of the central parsec of galaxies" (PID2020-114092GB-I00). The NASA/IPAC Extragalactic Database (NED) is funded by the National Aeronautics and Space Administration and operated by the California Institute of Technology.

References

- Alam, S., Albareti, F. D., Allende Prieto, C., et al. 2015, *ApJS*, 219, 12
 Bagchi, J., Sankhyayan, S., Sarkar, P., et al. 2017, *ApJ*, 844, 25
 Barber, C. B., Dobkin, D. P., & Huhdanpaa, H. 1996, *ACM Trans. Math. Softw.*, 22, 469
 Bond, J. R., Kofman, L., & Pogosyan, D. 1996, *Nature*, 380, 603
 Dabhade, P., Combes, F., Salomé, P., Bagchi, J., & Mahato, M. 2020a, *A&A*, 643, A111
 Dabhade, P., Gaikwad, M., Bagchi, J., et al. 2017, *MNRAS*, 469, 2886
 Dabhade, P., Mahato, M., Bagchi, J., et al. 2020b, *A&A*, 642, A153
 Dabhade, P., Röttgering, H. J. A., Bagchi, J., et al. 2020c, *A&A*, 635, A5
 Dabhade, P., Saikia, D. J., & Mahato, M. 2023, *Journal of Astrophysics and Astronomy*, 44, 13
 de Jong, R. S., Agertz, O., Berbel, A. A., et al. 2019, *The Messenger*, 175, 3
 DESI Collaboration, Adame, A. G., Aguilar, J., et al. 2023, arXiv e-prints, arXiv:2306.06308
 Einasto, J., Joeveer, M., & Saar, E. 1980, *MNRAS*, 193, 353
 Einasto, M., Einasto, J., Tenjes, P., et al. 2024, *A&A*, 681, A91
 Einasto, M., Kipper, R., Tenjes, P., et al. 2021, *A&A*, 649, A51
 Euclid Collaboration, Adam, R., Vannier, M., et al. 2019, *A&A*, 627, A23
 Fanaroff, B. L. & Riley, J. M. 1974, *MNRAS*, 167, 31P
 Garon, A. F., Rudnick, L., Wong, O. I., et al. 2019, *AJ*, 157, 126
 Horellou, C., Intema, H. T., Smolčić, V., et al. 2018, *A&A*, 620, A19
 Hutschenreuter, S., Anderson, C. S., Betti, S., et al. 2022, *A&A*, 657, A43
 Jackson, J. C. 1972, *MNRAS*, 156, 1P
 Kim, J., Park, C., L'Huillier, B., & Hong, S. E. 2015, *Journal of Korean Astronomical Society*, 48, 213
 Komberg, B. V. & Pashchenko, I. N. 2009, *Astronomy Reports*, 53, 1086
 Konar, C., Saikia, D. J., Ishwara-Chandra, C. H., & Kulkarni, V. K. 2004, *MNRAS*, 355, 845
 Kuźmicz, A., Czerny, B., & Wildy, C. 2019, *A&A*, 624, A91
 Lan, T.-W. & Prochaska, J. X. 2021, *MNRAS*, 502, 5104
 Lietzen, H., Tempel, E., Liivamägi, L. J., et al. 2016, *A&A*, 588, L4
 Liivamägi, L. J., Tempel, E., & Saar, E. 2012, *A&A*, 539, A80
 Liu, A., Bulbul, E., Kluge, M., et al. 2024, *A&A*, 683, A130
 Mack, K. H., Klein, U., O'Dea, C. P., Willis, A. G., & Saripalli, L. 1998, *A&A*, 329, 431
 Mauduit, J. C. & Mamon, G. A. 2007, *A&A*, 475, 169
 O'Dea, C. P. & Baum, S. A. 2023, *Galaxies*, 11, 67
 Oei, M. S. S. L., van Weeren, R. J., Gast, A. R. D. J. G. I. B., et al. 2023a, *A&A*, 672, A163
 Oei, M. S. S. L., van Weeren, R. J., Hardcastle, M. J., et al. 2024, arXiv e-prints, arXiv:2404.17776
 Oei, M. S. S. L., van Weeren, R. J., Hardcastle, M. J., et al. 2023b, *MNRAS*, 518, 240
 O'Sullivan, S. P., Brüggén, M., Van Eck, C. L., et al. 2018, *Galaxies*, 6, 126
 O'Sullivan, S. P., Machalski, J., Van Eck, C. L., et al. 2019, *A&A*, 622, A16
 O'Sullivan, S. P., Shimwell, T. W., Hardcastle, M. J., et al. 2023, *MNRAS*, 519, 5723
 Pillastrini, G. C. B. 2019, *New A*, 69, 1
 Planck Collaboration, Aghanim, N., Akrami, Y., et al. 2020, *A&A*, 641, A6
 Raychaudhury, S. 1989, *Nature*, 342, 251
 Rudnick, L. & Blundell, K. M. 2003, *ApJ*, 588, 143
 Safouris, V., Subrahmanyan, R., Bicknell, G. V., & Saripalli, L. 2009, *MNRAS*, 393, 2
 Sankhyayan, S., Bagchi, J., Tempel, E., et al. 2023, *ApJ*, 958, 62
 Shimwell, T. W., Hardcastle, M. J., Tasse, C., et al. 2022, *A&A*, 659, A1
 Simonte, M., Andernach, H., Brüggén, M., Best, P. N., & Osinga, E. 2023, *A&A*, 672, A178
 Simonte, M., Andernach, H., Brüggén, M., et al. 2022, *MNRAS*, 515, 2032
 Strom, R. G. 1973, *A&A*, 25, 303
 Vanderwoude, S., West, J. L., Gaensler, B. M., et al. 2024, *AJ*, 167, 226
 Venturi, T., Giacintucci, S., Merluzzi, P., et al. 2022, *A&A*, 660, A81
 Wen, Z. L. & Han, J. L. 2015, *ApJ*, 807, 178
 Xu, Y., Kronberg, P. P., Habib, S., & Dufton, Q. W. 2006, *ApJ*, 637, 19
 York, D. G., Adelman, J., Anderson, Jr., J. E., et al. 2000, *AJ*, 120, 1579

Appendix A: Sky Masks

Fig. A.1 shows the locations of GRGs within superclusters and the sky-masks associated with the SCl-catalogue and GRG-catalogue.

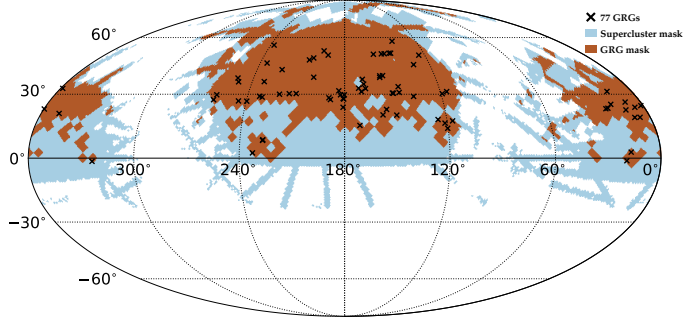


Fig. A.1: Sky footprints of the GRG-catalogue and the SCl-catalogue. The sky coverage of the intersection of the two masks is considered for the analysis in this paper.

Appendix B: Identification of giant radio galaxies in clusters

The cluster membership of a GRG host should be treated carefully because the peculiar velocities of GRGs within a cluster can impact the identification of GRGs residing in a cluster environment. The fingers-of-god redshift distortions, induced by the peculiar velocities, may displace a member galaxy of a cluster outside the cluster's virial radius (R_{200} ; the radius of a sphere in which the matter density is 200 times higher than the critical density of the Universe) in the redshift space. Utilizing the virial mass (M_{200}) of a cluster, we derived the velocity dispersion ($\sigma_v = \sqrt{GM_{200}/3R_{200}}$) induced along the line of sight. Our approach involves the initial identification of GRGs within the projected R_{200} on the sky plane, followed by the identification of GRGs within the redshift range ($\bar{z} \pm \Delta z$; $\Delta z = \sigma_v(1 + \bar{z})/c$) associated with cluster peculiar velocities. Here \bar{z} and c are the mean redshift of the cluster and the speed of light, respectively. Such GRGs are considered to be members of clusters. Among these GRGs, those lying within $3''$ of the brightest cluster galaxy (BCG) are labelled BCG while the remaining ones are labelled Mem-C1. GRGs failing to meet these criteria are labelled No-C1. Corrections to the comoving distance of GRGs within a cluster to suppress the fingers-of-god redshift distortions are then done as

$$d_{\text{GRG,corr}} = d_{\text{Cl}} + (d_{\text{GRG}} - d_{\text{Cl}}) \frac{R_{200}}{(\sigma_v/H_0)}.$$

Here $d_{\text{GRG,corr}}$ is the corrected comoving distance to the GRG, d_{GRG} is the uncorrected comoving distance to the GRG, and d_{Cl} is the comoving distance to the cluster (Liivamägi et al. 2012; Bagchi et al. 2017).

Appendix C: Distance of giant radio galaxies from the nearest member cluster

Fig. C.1 shows the distance to the nearest clusters and the sizes of GRGs within superclusters.

Appendix D: Magnetic field estimation

Polarised electromagnetic radiation undergoes Faraday rotation when it passes through a magnetized plasma, resulting in a rotation measure (RM) determined by the equation $\text{RM} =$

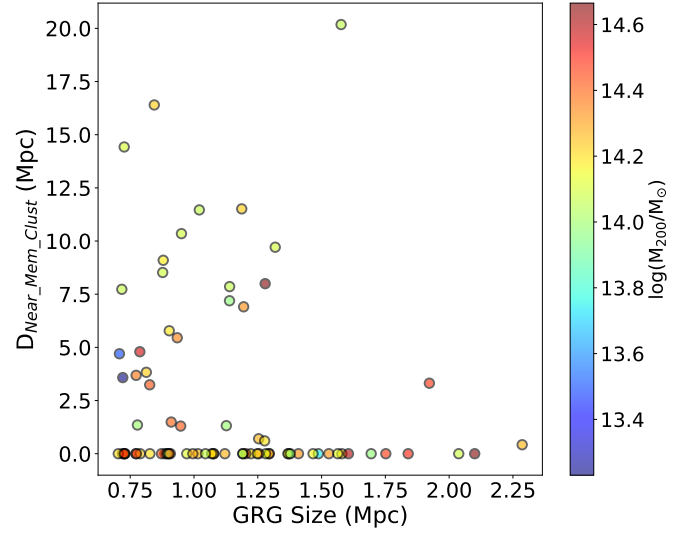


Fig. C.1: Distance of GRGs (inside superclusters) from their nearest member cluster as a function of their size. The galaxy cluster mass is colour-coded. Data points located in the lowest region ($D_{\text{Near_Mem_Clust}} = 0$) of the graph correspond to BCG-GRGs (GRGs that are BCGs).

$0.81 \int_0^L n_e B_{\parallel} dl$, where B_{\parallel} is the magnetic field component along the line of sight. The constant 0.81 is derived from physical constants in appropriate units, where RM , n_e , B_{\parallel} , and dl are given in units of rad m^{-2} , cm^{-3} , μG , and parsec, respectively; \int_0^L represents the integral from 0 to L , where L is the total path length; n_e is the thermal electron number density; and dl is the path length element. In the case of polarised light from a GRG traversing through a supercluster (in addition to the discussion in Sect. 5), we assume uniform n_e and B_{\parallel} within the supercluster and negligible magnetic field effects in a non-supercluster environment. Based on this, an estimate of magnetic field strength can be derived as $B_{\parallel} = \text{RM}/(0.81 n_e \Delta L)$. Here $\Delta L = \Delta L_{\parallel, \text{SCl}}$ and represents the path length covered by the polarised light within the supercluster (see illustration shown in Fig. D.1). This estimation provides insights into the magnetic field strength in superclusters under simplified conditions. These simplified conditions are applied to estimate the magnetic field inside a supercluster (also see Table E.2). The RM values from O'Sullivan et al. (2023) have been corrected for the contribution from the galactic RM based on Hutschenreuter et al. (2022), and hence they are referred to as residual rotation measure or RRM.

As shown in Table E.2, SCl 391 and 658 each have two entries. In both cases, these measurements pertain to a single GRG, with data derived from its two lobes, whose RRM's vary notably. This variation can arise from several factors. Firstly, the local environments around each lobe may differ in magnetic field strengths and n_e , resulting in varying degrees of Faraday rotation. Secondly, the polarised light from each lobe may traverse different intervening media, such as galaxy clusters, filaments, or voids, with differing magnetic field strengths and n_e . Additionally, intrinsic differences within the lobes themselves, such as variations in magnetic field structure or plasma density, could contribute to the observed RM differences. The most likely scenario is that the polarised light from the lobes encounters significantly different intervening media, as each line of sight can intersect diverse large-scale structures (e.g. a supercluster) with varying magnetic field strength and electron densities.

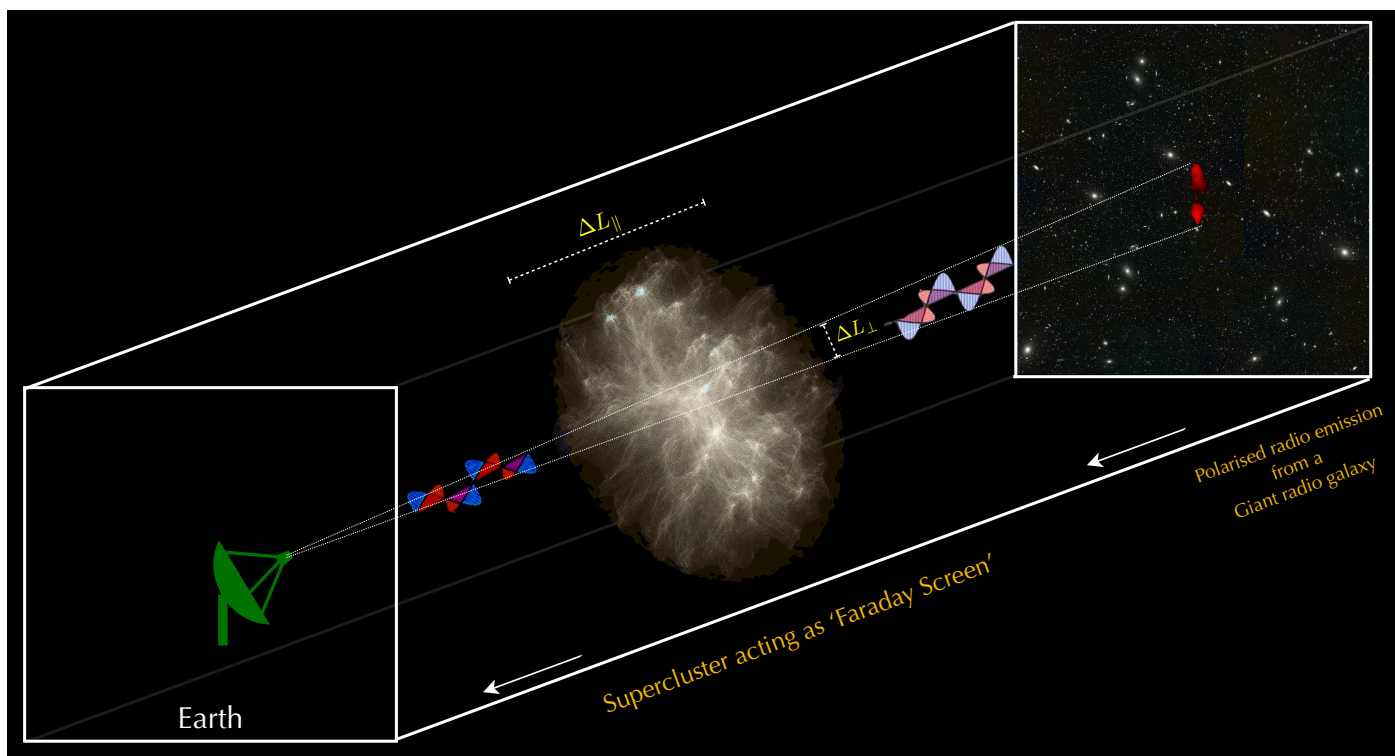


Fig. D.1: Polarised light propagation through the supercluster's magneto-ionic medium, illustrating the resultant Faraday rotation prior to detection by terrestrial telescopes (see Sect. 5).

Appendix E: Tables

Table E.1: Properties of 77 GRGs and their host superclusters.

SCl	RA _{SCl} (deg)	Dec _{SCl} (deg)	z _{SCl}	CoSize _{SCl} (Mpc)	Mass _{SCl} (10 ¹⁴ M _⊙)	NMem _{SCl}	δ _{SCl}	RA _{GRG} (deg)	Dec _{GRG} (deg)	z _{GRG}	Size _{GRG} (Mpc)	Env _{GRG}
(1)	(2)	(3)	(4)	(5)	(6)	(7)	(8)	(9)	(10)	(11)	(12)	(13)
2	235.1322	28.2855	0.0792	123.59	255.2	57	3.12	230.8622	28.6257	0.0808	1.08	BCG
2	235.1322	28.2855	0.0792	123.59	255.2	57	3.12	239.6893	26.6477	0.0861	1.02	No-Cl
2	235.1322	28.2855	0.0792	123.59	255.2	57	3.12	232.5428	29.0084	0.0847	0.72	BCG
15	196.9778	52.5004	0.2764	121.59	151.7	28	4.36	195.8841	52.3339	0.2720	0.84	No-Cl
35	190.7367	29.0072	0.2329	83.96	127.5	31	3.88	188.6948	27.4276	0.2278	0.97	BCG
35	190.7367	29.0072	0.2329	83.96	127.5	31	3.88	189.6500	28.2643	0.2358	0.95	No-Cl
38	176.4949	22.7656	0.1770	98.21	123.7	30	9.48	180.9321	23.7180	0.1766	0.73	BCG
51	6.9235	19.1288	0.4053	126.32	111.3	21	1.57	5.9896	18.9822	0.4062 [†]	1.58	No-Cl
53	203.1943	48.3906	0.3306	79.58	110.9	24	5.35	202.6742	48.4652	0.3317	0.72	No-Cl
66	222.5309	41.0626	0.3360	68.52	105.0	22	8.45	222.8934	42.3150	0.3305	1.30	BCG
73	180.3112	26.4533	0.1386	94.41	101.7	21	7.23	180.5432	27.6858	0.1353	1.69	BCG
73	180.3112	26.4533	0.1386	94.41	101.7	21	7.23	182.5342	29.7387	0.1430	0.90	No-Cl
73	180.3112	26.4533	0.1386	94.41	101.7	21	7.23	180.9027	27.9442	0.1398	0.89	BCG
74	227.2883	6.2860	0.0794	74.83	100.5	20	19.66	226.9918	8.2052	0.0775	0.73	BCG
74	227.2883	6.2860	0.0794	74.83	100.5	20	19.66	226.8555	8.4957	0.0787	0.79	No-Cl
81	145.0124	31.7802	0.3869	113.02	97.1	24	1.10	145.8632	30.8688	0.3999	1.53	BCG
88	125.9072	18.2376	0.3009	106.99	93.7	21	7.56	125.1783	17.9105	0.2963	1.12	BCG
92	349.1767	20.9235	0.1016	112.99	92.6	23	5.18	349.3324	20.7911	0.1028	0.73	No-Cl
94	166.9559	33.3516	0.2499	70.15	92.4	20	11.89	166.7532	32.7736	0.2478	1.37	BCG
94	166.9559	33.3516	0.2499	70.15	92.4	20	11.89	167.7293	35.0032	0.2534	1.22	BCG
95	152.8222	31.6474	0.3048	133.11	92.3	24	1.51	150.1840	30.5782	0.3076	1.32	No-Cl
101	128.9984	44.5972	0.1481	83.52	91.2	27	4.37	131.3629	44.9240	0.1506	0.81	No-Cl
110	22.4893	22.3887	0.2338	73.07	89.5	23	4.27	23.5116	23.0341	0.2412 [†]	1.37	BCG
110	22.4893	22.3887	0.2338	73.07	89.5	23	4.27	22.1410	23.2747	0.2343	1.02	BCG
139	323.7062	-1.6868	0.3190	95.34	82.9	15	15.65	323.7409	-1.4716	0.3192	1.41	BCG

Continued on next page

Table E.1 – Continued from previous page

SCI	RA _{SCI}	Dec _{SCI}	z _{SCI}	CoSize _{SCI}	Mass _{SCI}	NMem _{SCI}	δ _{SCI}	RA _{GRG}	Dec _{GRG}	z _{GRG}	Size _{GRG}	Env _{GRG}
(1)	(deg)	(deg)	(4)	(Mpc)	($10^{14} M_{\odot}$)	(7)	(8)	(deg)	(deg)	(11)	(Mpc)	(13)
142	248.9777	35.5225	0.1630	63.87	81.8	21	7.26	250.3455	38.0360	0.1630	2.10	BCG
142	248.9777	35.5225	0.1630	63.87	81.8	21	7.26	248.8438	36.1347	0.1650	0.93	No-Cl
144	120.4256	30.2375	0.3203	78.41	81.5	16	5.68	119.1836	30.2619	0.3246	1.08	BCG
148	147.2374	51.2899	0.2143	63.76	80.5	15	8.53	146.1975	51.1037	0.2132	1.20	BCG
148	147.2374	51.2899	0.2143	63.76	80.5	15	8.53	145.0158	51.0727	0.2102	0.91	BCG
154	231.7755	35.6210	0.2311	67.60	78.2	17	28.90	232.2368	36.2281	0.2263	1.19	BCG
162	116.9295	17.0322	0.1861	51.98	77.4	16	14.16	116.7848	17.2907	0.1876	1.07	BCG
170	259.8995	29.7333	0.1998	68.57	76.1	14	12.76	259.3549	29.7258	0.1995	0.88	No-Cl
176	9.6464	24.5548	0.1490	75.77	75.4	21	4.65	9.3298	26.2201	0.1477	1.38	BCG
185	154.9045	20.2379	0.1131	70.43	74.1	20	6.20	157.2733	20.1117	0.1110	1.25	Mem-Cl
185	154.9045	20.2379	0.1131	70.43	74.1	20	6.20	154.9072	22.7011	0.1121	0.87	BCG
198	17.9861	-1.3457	0.1842	78.48	71.3	18	9.67	19.3952	-1.1932	0.1855	1.19	No-Cl
208	207.1101	48.4068	0.1683	60.80	70.0	21	6.54	205.5291	47.4314	0.1721	1.29	BCG
239	156.0541	49.9667	0.1572	47.54	65.6	12	32.64	158.3127	50.4854	0.1610	0.89	BCG
243	358.6942	21.2500	0.1702	66.84	65.0	16	7.70	359.7640	22.9057	0.1743	1.04	BCG
247	220.0690	29.9014	0.3184	56.48	64.4	12	18.81	220.5093	30.0196	0.3185	1.58	BCG
255	259.9947	29.9550	0.1063	67.98	63.7	18	5.11	260.2201	27.3553	0.1038	0.90	BCG
270	15.8345	2.0067	0.1982	66.00	62.3	20	7.36	16.8451	2.7823	0.1957	1.49	BCG
282	171.0924	16.2980	0.1722	98.65	61.6	17	4.58	171.0949	15.1661	0.1719	0.70	BCG
292	9.2388	18.5378	0.1484	47.97	61.0	12	41.58	9.1443	18.9015	0.1508 [†]	1.84	BCG
324	115.7264	31.1060	0.3354	64.58	58.5	11	7.23	116.0027	31.2913	0.3408	1.92	No-Cl
327	18.0800	25.0406	0.1853	64.14	58.2	18	9.36	18.9885	25.1223	0.1837	1.28	BCG
355	168.9547	31.4473	0.2211	47.24	55.8	12	20.41	169.4294	31.2801	0.2206	1.28	No-Cl
357	200.2504	38.0586	0.2380	65.29	55.7	12	21.91	200.4425	38.4360	0.2380	0.91	Mem-Cl
359	150.1405	50.9867	0.3997	82.69	55.6	15	3.63	150.0645	50.7491	0.3990	0.77	No-Cl
391	208.7158	27.2658	0.0626	71.41	53.6	15	18.87	214.4777	30.2685	0.0633	0.78	Mem-Cl
400	190.9292	50.2206	0.3558	54.18	53.0	12	11.85	192.3050	50.0121	0.3559	1.25	BCG
403	0.0314	24.6204	0.3865	107.36	52.8	14	7.70	1.3556	24.5018	0.3874	1.47	BCG
418	155.3968	39.5241	0.1485	52.16	51.9	12	66.98	154.6892	39.2498	0.1482	2.04	BCG
418	155.3968	39.5241	0.1485	52.16	51.9	12	66.98	156.5953	39.1477	0.1485	1.75	BCG
422	158.0902	36.0347	0.1227	39.39	51.7	10	42.60	156.7660	38.3370	0.1243	1.00	BCG
430	170.1028	37.6143	0.1048	57.95	51.0	19	13.90	168.3905	37.3744	0.1028	0.73	BCG
446	236.1536	54.7598	0.2873	74.11	49.7	11	6.66	237.3650	55.6129	0.2936	1.28	Mem-Cl
460	12.6146	22.7254	0.1830	63.18	48.7	12	13.59	11.9653	22.4580	0.1831	1.56	BCG
462	125.2028	49.3166	0.1572	67.25	48.7	13	26.71	124.4002	49.9923	0.1591	1.19	BCG
476	231.6128	1.8272	0.3286	79.55	47.3	10	4.85	232.4616	2.4209	0.3252	0.83	BCG
478	357.2936	33.3015	0.3335	62.58	47.1	10	20.55	358.6730	32.8827	0.3415	2.29	Mem-Cl
504	235.1780	46.9601	0.2021	40.50	45.4	13	20.80	235.1880	45.7572	0.2045	1.25	BCG
506	15.5556	31.3543	0.2208	45.84	45.0	11	50.95	15.3901	31.3678	0.2198	1.61	BCG
512	138.5962	28.9773	0.1807	64.88	44.4	19	6.68	137.3706	28.9551	0.1821	1.14	No-Cl
525	178.8038	29.7090	0.1562	71.05	43.5	12	12.84	180.1921	29.7160	0.1606	0.77	BCG
560	170.0182	33.0557	0.2079	66.33	40.9	14	7.75	171.1136	32.9353	0.2062	0.88	No-Cl
582	149.6766	30.3924	0.3188	59.67	38.9	10	7.25	149.5718	30.4783	0.3223	1.19	No-Cl
586	149.0897	20.0109	0.1709	48.20	38.7	11	17.12	149.1462	19.9985	0.1725	1.13	Mem-Cl
604	181.6674	31.7969	0.2027	52.81	37.2	13	7.27	183.6326	31.6832	0.2020	0.95	Mem-Cl
615	120.2823	16.1700	0.1050	61.62	36.2	14	7.61	120.2556	13.8312	0.1076	0.90	BCG
615	120.2823	16.1700	0.1050	61.62	36.2	14	7.61	121.4295	16.2322	0.1000	0.79	BCG
623	151.7800	50.8995	0.2252	43.27	35.2	10	23.39	152.2168	50.7002	0.2245	1.14	No-Cl
626	144.9063	33.0645	0.1290	44.17	34.8	10	38.47	145.8875	33.6995	0.1314	0.83	No-Cl
634	244.6070	29.7925	0.0960	70.18	33.3	11	13.27	244.7787	26.7573	0.0963	0.71	No-Cl
658	5.5670	21.8839	0.0987	68.59	26.0	10	16.20	5.5914	23.7337	0.0979 [†]	0.77	BCG
659	132.7396	60.3174	0.1326	78.22	25.9	10	15.41	139.9519	57.8489	0.1370	0.72	No-Cl

Notes. The subscripts ‘SCI’ and ‘GRG’ indicate host supercluster and GRG properties, respectively. Column 1 (SCI) is the supercluster identification number from [SSC23](#). The other columns include RA, Dec (right ascension and declination), z (redshift), CoSize (comoving size), Size (projected physical size), Mass (supercluster mass), NMem (number of member clusters), and δ (density contrast of the supercluster). The coordinates of GRGs (3 in each) located in SCI 2 (see Fig. 1) and SCI 73 are highlighted in bold. The last column, Env_{GRG}, categorises the environment of the GRG: BCG indicates the GRG is central within a BCG-hosted galaxy cluster (47 sources), No-Cl denotes GRGs outside any galaxy cluster (23 sources), and Mem-Cl signifies GRGs residing within a galaxy cluster (7 sources) that are not BCGs. z_{GRG} with [†] indicates photometric redshift. Redshift information for GRGs has been sourced from their respective reporting catalogues, which are primarily derived from the SDSS ([York et al. 2000](#)).

Table E.2: Details of eight GRGs identified in the background of the superclusters with their respective properties.

SCI	RA _{SCI} (deg)	Dec _{SCI} (deg)	z _{SCI}	RA _{GRG} (deg)	Dec _{GRG} (deg)	z _{GRG}	Cat-ID	RRM _{GRG} (rad m ⁻²)	ΔL _{∥,SCI} (Mpc)	Δz _{SCI}	ΔL _{⊥,SCI} (kpc)	B _{∥,SCI} (n _{e1} , n _{e2}) (μG)
(1)	(2)	(3)	(4)	(5)	(6)	(7)	(8)	(9)	(10)	(11)	(12)	(13)
2	235.1322	28.2855	0.0792	227.24375	28.44117	0.35837	3015	-0.18	110	0.0279	67	0.002 0.020
92	349.1767	20.9235	0.1016	352.08936	21.76098	0.13186	9264	2.78	51	0.0132	233	0.068 0.678
92	349.1767	20.9235	0.1016	352.02502	19.35509	0.18719	9254	-2.74	51	0.0132	274	0.067 0.669
176	9.6464	24.5548	0.1490	9.11250	25.61799	0.23348	20	-5.27	61	0.0171	108	0.106 1.064
265	204.8944	39.4580	0.1692	205.67650	38.88794	0.25576	994	-2.89	40	0.0115	52	0.089 0.891
265	204.8944	39.4580	0.1692	205.72708	37.97167	0.23700	7471	0.81	40	0.0115	54	0.025 0.252
391	208.7158	27.2658	0.0626	210.18083	30.32194	0.20604	15905	-0.82	23	0.0056	199	0.045 0.446
391	208.7158	27.2658	0.0626	210.18083	30.32194	0.20604	7540	3.00	23	0.0056	89	0.164 1.639
658	5.5670	21.8839	0.0987	4.56337	21.69262	0.30256	3621	-1.32	32	0.0083	95	0.051 0.513
658	5.5670	21.8839	0.0987	4.56337	21.69262	0.30256	3620	-5.19	32	0.0083	104	0.201 2.014

Notes. The subscripts ‘SCI’ and ‘GRG’ indicate foreground supercluster and background GRG properties, respectively. The columns RA, Dec, and z are the right ascension, declination, and redshift, respectively. Cat-ID refers to the ID source number from the catalogue of O’Sullivan et al. (2023). RRM_{GRG} stands for residual rotation measure (the value of rotation measure after correcting for the galactic magnetic field contribution), ΔL_{∥,SCI} is the path length covered by the polarised light (from the background GRG) inside the supercluster, ΔL_{⊥,SCI} is the approximate projected length of the polarised emission from the background GRG on the supercluster, and Δz_{SCI} is the redshift width of the supercluster. B_{∥,SCI} is the estimated magnetic field in the supercluster for n_{e1} and n_{e2} corresponding to the n_e values of 10⁻⁶ cm⁻³ and 10⁻⁷ cm⁻³, respectively (see Sect. 5 and Appendix D for further details).